Chiral evolution and femtoscopic signatures of the $K_1(1270)$ resonance

Jia-Ming Xie,[1,2] Zhi-Wei Liu,[1] Jun-Xu Lu,[1,*] Haozhao Liang,[2,3,4,†] Raquel Molina,[5,‡] and Li-Sheng Geng[6,1,7,8,9,§]

[1]*School of Physics, Beihang University, Beijing 102206, China*
[2]*Department of Physics, Graduate School of Science, The University of Tokyo, Tokyo 113-0033, Japan*
[3]*Quark Nuclear Science Institute, The University of Tokyo, Tokyo 113-0033, Japan*
[4]*RIKEN Center for Interdisciplinary Theoretical and Mathematical Sciences, Wako 351-0198, Japan*
[5]*Departamento de Física Teórica and IFIC, Centro Mixto Universidad de Valencia-CSIC, Parc Científic UV, C/ Catedrático José Beltrán, 2, 46980 Paterna, Spain*
[6]*Sino-French Carbon Neutrality Research Center, École Centrale de Pékin/School of General Engineering, Beihang University, Beijing 100191, China*
[7]*Peng Huanwu Collaborative Center for Research and Education, Beihang University, Beijing 100191, China*
[8]*Beijing Key Laboratory of Advanced Nuclear Materials and Physics, Beihang University, Beijing 102206, China*
[9]*Southern Center for Nuclear-Science Theory (SCNT), Institute of Modern Physics, Chinese Academy of Sciences, Huizhou 516000, China*

(Received 20 November 2025; accepted 6 February 2026; published 1 April 2026)

We present a comprehensive study of the axial-vector resonance $K_1(1270)$ within the unitarized chiral perturbation theory, focusing on its two-pole structure and manifestation in femtoscopic observables. By considering the dominant ρK and $K^*\pi$ coupled channels, we reproduce the well-established double-pole structure and trace the chiral evolution of both poles as functions of the pion mass, using the vector-meson mass trajectories fitted to lattice-QCD data and experimental values. The lower pole, dominantly coupled to $K^*\pi$, evolves from an above-threshold resonance to a virtual or bound state with increasing pion mass. In comparison, the higher pole, dominantly coupled to ρK, moves downward in energy, reflecting the strengthening of the chiral attraction. The influence of the finite vector-meson widths is systematically examined, showing that their inclusion smooths the pole trajectories without altering their qualitative behavior. Furthermore, femtoscopic correlation functions are calculated for all relevant vector-pseudoscalar channels in both charged sectors. The results exhibit distinct resonance and bound-state features consistent with the two-pole dynamics. The weak impact of higher channels, such as $\omega\bar{K}$, $\bar{K}^*\eta$, and $\phi\bar{K}$, confirms that the simplified two-channel treatment captures the essential dynamics of the $K_1(1270)$ resonance. This study demonstrates that combining chiral extrapolation and femtoscopic correlation analyses provides a powerful and complementary framework for connecting lattice-QCD calculations, chiral effective theory, and experimental measurements, offering new insights into the molecular nature and chiral origin of the $K_1(1270)$ resonance.

DOI: 10.1103/cnqj-dvqj

I. INTRODUCTION

Understanding the internal structure of hadronic resonances remains one of the most challenging problems in nonperturbative QCD [1–13]. Among them, the low-lying axial-vector mesons, such as $a_1(1260)$, $f_1(1285)$, and $K_1(1270)$ [14,15], provide an essential probe into chiral symmetry breaking and the dynamics of vector-pseudoscalar (VP) interactions. In the conventional quark model [16], these resonances are described as the $L = 1$ orbital excitations of $q\bar{q}$ states, forming the 1^3P_1 and 1^1P_1 nonets. The strange partners $K_1(1270)$ and $K_1(1400)$ are usually interpreted as mixtures of the SU(3) eigenstates K_{1A} ($C = +1$) and K_{1B} ($C = -1$) due to SU(3)-flavor symmetry breaking.

However, certain long-standing experimental inconsistencies—such as reaction-dependent line shapes, channel-dependent branching ratios ($K^*\pi$ vs ρK), and interference with $K_1(1400)$—challenge this simple mixing picture [17]. The coexistence of multiple peaks in diffractive and nondiffractive Kp reactions suggests that the internal

*Contact author: ljxwohool@buaa.edu.cn
†Contact author: haozhao.liang@phys.s.u-tokyo.ac.jp
‡Contact author: Raquel.Molina@ific.uv.es
§Contact author: lisheng.geng@buaa.edu.cn

Published by the American Physical Society under the terms of the Creative Commons Attribution 4.0 International license. Further distribution of this work must maintain attribution to the author(s) and the published article's title, journal citation, and DOI. Funded by SCOAP³.

structure of $K_1(1270)$ is more complex than a single Breit-Wigner resonance [11].

The development of unitarized chiral perturbation theory (UChPT) provides a compelling alternative [18–24]. By unitarizing chiral VP interactions [15,25], UChPT dynamically generates axial-vector states as hadronic molecules rather than conventional $q\bar{q}$ excitations. Notably, UChPT [15] predicted two nearby poles associated with $K_1(1270)$, originating from the coupled-channel dynamics among $K^*\pi$, ρK, ωK, $K^*\eta$, and ϕK. The analysis of the high-statistics WA3 data on $K^-p \to K^-\pi^+\pi^-p$ [17] further supports the existence of two poles: a lower one around $1195 - 123i$ MeV dominantly coupling to $K^*\pi$, and a higher one around $1284 - 73i$ MeV mainly coupling to ρK. This provided strong evidence that $K_1(1270)$ is a superposition of two dynamically generated states rather than a simple K_{1A}–K_{1B} mixture.

Subsequent studies reinforced this picture. Wang *et al.* [26] analyzed $D^0 \to \pi^+ VP$ decays, showing that different final states manifest different poles—$K^*\pi$ the lower one, and ρK the higher. Later, their study of semileptonic $D^+ \to \nu e^+ VP$ decays [27] confirmed this channel dependence. Dias *et al.* [28] extended the analysis to $\bar{B} \to J/\psi\rho\bar{K}$ and $\bar{B} \to J/\psi\bar{K}^*\pi$, finding both poles in the line shapes of the ρK and $K^*\pi$ spectra. Roca *et al.* [29] further showed that the particle data group branching ratios for $K_1(1270) \to \pi K_0^*(1430)$ [30] are inconsistent with a single-state interpretation, reinforcing the two-pole picture.

Together, these theoretical and phenomenological studies establish a coherent framework in which the $K_1(1270)$ resonance emerges as two dynamically generated poles arising from vector-pseudoscalar interactions—an analog of the well-known two-pole nature of the $\Lambda(1405)$ [31–37]. Despite these advances, direct experimental confirmation remains elusive, and the dependence of the pole structure on light-quark masses—crucial for connecting lattice QCD simulations to experiments—has yet to be systematically explored [38–41].

Meanwhile, the two-particle femtoscopic correlation technique has become a quantitative and model-sensitive probe of hadron-hadron interactions at low relative momenta [13,42–59]. Femtoscopy provides direct access to scattering lengths, effective ranges, and near-threshold resonance structures that are otherwise unreachable in conventional scattering experiments. Kamiya *et al.* [42] achieved a major step forward by developing a coupled-channel femtoscopic framework for the K^-p system considering the $\bar{K}N - \pi\Sigma - \pi\Lambda$ dynamics based on chiral SU(3) theory. Their results, including Coulomb and coupled-channel effects, successfully reproduced the ALICE K^-p correlation data, providing stringent empirical constraints on the $\bar{K}N$ interaction responsible for the $\Lambda(1405)$. Following this, Liu *et al.* [47] extended the approach to the DK system, showing that theoretically predicted correlation functions (CFs) are consistent with interpreting the $D_{s0}^*(2317)$ as a hadronic molecule dynamically generated from the DK interaction, and highlighting that future femtoscopic measurements could directly test this scenario.

Given these developments, applying the femtoscopic framework to the VP interactions offers a natural and timely opportunity to probe the exotic resonance $K_1(1270)$. Since direct ρK and $K^*\pi$ scattering measurements are experimentally inaccessible due to the short lifetimes of vector mesons, information on $K_1(1270)$ must be inferred from the $K\pi\pi$ invariant-mass spectra [17,26,27], where the coupled VP subsystems act as intermediate states. In contrast, femtoscopy provides a direct means of accessing the underlying two-body interaction kernels via near-threshold correlation-function observables. A systematic study of VP femtoscopic CFs across different channels can thus provide crucial constraints on the two-pole dynamics of $K_1(1270)$ and yield new insights into its internal structure and chiral origin.

In this work, we present a quantitative study of the $K_1(1270)$ resonance within the two-pole scenario, combining chiral extrapolation and femtoscopic CF analyses. First, we employ UChPT to trace the mass evolution of the two poles as a function of the pion mass, linking theoretical predictions to future lattice-QCD simulations. Second, we analyze femtoscopic CFs of VP systems to probe near-threshold interactions and assess the impact of the two poles on observable correlation functions.

The paper is organized as follows. Section II A outlines the theoretical framework of VP interactions in UChPT and presents the extrapolation formulas for vector-meson masses. Section II B introduces the formalism of femtoscopic CFs and their application to the VP system. In Sec. III A, we fit the chiral trajectories of the vector mesons ρ and K^* using lattice-QCD and experimental data, followed by an analysis of the two-pole evolution with increasing pion mass in Sec. III B. Section III C presents the computed femtoscopic CFs for various coupled channels. Finally, Sec. IV summarizes our findings and outlines prospects for future theoretical and experimental studies.

II. FORMALISM

A. UChPT and mass evolution

For the VP interaction, the leading-order (LO) chiral Lagrangian [15,25] takes the following form

$$\mathcal{L}_{\rm VP}^{\rm WT} = -\frac{1}{4f^2}\mathrm{Tr}([\mathcal{V}^\mu, \partial^\nu \mathcal{V}_\mu][\Phi, \partial_\nu \Phi]), \tag{1}$$

from which one obtains the Weinberg-Tomozawa (WT) interaction kernel, projected onto the S wave, which reads [15,17]

$$V_{ij}(s) = -\epsilon^i \cdot \epsilon^j \frac{C_{ij}}{8f^2}\Big[3s - (M_i^2 + m_i^2 + M_j^2 + m_j^2) - \frac{1}{s}(M_i^2 - m_i^2)(M_j^2 - m_j^2)\Big], \quad (2)$$

where C_{ij} are the channel-dependent coupling coefficients determined by SU(3) symmetry [15,17], f is the decay constant, M and m are the masses of the vector and pseudoscalar mesons, respectively, and ϵ^i (ϵ^j) denotes the polarization vector of the initial (final) vector meson.

Within the UChPT [22], the on-shell unitarized scattering amplitude is given by

$$T = (1 - VG)^{-1}V, \quad (3)$$

where G is a diagonal matrix whose elements $G_i(\sqrt{s})$ correspond to the loop functions of the individual coupled channels. In this work, the logarithmic divergence of $G_i(\sqrt{s})$ is regularized using the dimensional-regularization scheme, which ensures a proper analytic continuation to higher energies. To study the resonance properties, we look for the complex pole positions z_R on the second Riemann sheet [11,60,61] The couplings g_i of these poles to various channels are then obtained from the residues at z_R as $T_{ij}(s) = \lim_{s\to z_R} g_i g_j/(s - z_R)$. Further details of this formalism can be found in Ref. [22].

An important refinement arises when dealing with intermediate states containing unstable particles with sizable decay widths. In such cases, the standard loop functions need to be modified to account for the finite-width effects, which can be consistently incorporated through the Källén-Lehmann spectral representation of the vector-meson propagators as

$$\tilde{G}_i(\sqrt{s}) = \frac{1}{C}\int_{(M_V-2\Gamma_V)^2}^{(M_V+2\Gamma_V)^2} ds_V\, G_i(\sqrt{s}, \sqrt{s_V}, m_i) \times \left(-\frac{1}{\pi}\right) \mathrm{Im}\left\{\frac{1}{s_V - M_V^2 + iM_V\Gamma_V}\right\}, \quad (4)$$

where the normalization factor C is given by

$$C = \int_{(M_V-2\Gamma_V)^2}^{(M_V+2\Gamma_V)^2} ds_V \left(-\frac{1}{\pi}\right) \mathrm{Im}\left\{\frac{1}{s_V - M_V^2 + iM_V\Gamma_V}\right\}. \quad (5)$$

This treatment effectively replaces the narrow-width approximation and leads to a more realistic description of the VP dynamics, as discussed in Refs. [15,17].

We now turn to the chiral extrapolation of the masses of the relevant particles involved in the ρK and $K^*\pi$ coupled-channel system. As the pion mass increases, the square of the kaon mass approximately follows a linear relation in terms of m_π^2, which can be expressed as

$$m_K^2 = a + bm_\pi^2 + ca_{\mathrm{lat}}^2, \quad (6)$$

where the coefficients a, b, and c are determined by fitting to the lattice-QCD and experimental data. This form is consistent with the standard chiral extrapolation of pseudoscalar meson masses [62].

For the vector mesons, both the ρ and K^* masses, as well as their coupling constants g_{VPP} relevant to the dominant decay channels $\rho \to \pi\pi$ and $K^* \to \pi K$, are parametrized in a similar quadratic form [63–65],

$$m_{\mathrm{V}} = c_0 + c_1 m_\pi^2 + c_2 a_{\mathrm{lat}}^2, \quad g_{\mathrm{VPP}} = \tilde{c}_0 + \tilde{c}_1 m_\pi^2 + \tilde{c}_2 a_{\mathrm{lat}}^2, \quad (7)$$

where the coefficients $(c_i, \tilde{c}_i)$ are obtained from global fits combining lattice-QCD results and experimental data. Furthermore, the decay width for the $\rho \to \pi\pi$ decay channel can be written as

$$\Gamma_\rho = \frac{g_{\rho\pi\pi}^2}{6\pi m_\rho^2}\left(\frac{m_\rho^2}{4} - m_\pi^2\right)^{3/2}, \quad (8)$$

and an analogous expression holds for the $K^* \to \pi K$ decay. In particular, our treatment in Eq. (7) reproduces the IR-regularized chiral effective field theory (EFT) result under the same truncation-keeping terms up to $\mathcal{O}(m_\pi^2)$ and discarding higher-order/nonanalytic pieces [66]. Finally, the inclusion of the a_{lat}^2 term effectively accounts for finite-lattice-spacing artifacts up to $\mathcal{O}(a_{\mathrm{lat}}^2)$ and ensures a smooth extrapolation to the continuum limit [64].

Note that the ρ and K^* mesons can be dynamically generated within the chiral unitary approach or the inverse-amplitude method by employing the chiral Lagrangians for meson-meson scattering, as demonstrated in Refs. [67,68]. The pion-mass dependence of the ρ meson has been investigated in this framework in Refs. [69–71]. In the present work, we focus on tracing the movement of the pole dynamically generated by the WT term of Eq. (2) in the VP meson interaction. For this purpose, a simplified parametrization of the pion-mass dependence of the ρ and K^* mesons is sufficient.

B. Femtoscopic correlation functions

The femtoscopic CF provides a powerful means of extracting information on hadron-hadron interactions at low relative momenta from two-particle momentum correlations. Within the standard Koonin-Pratt formalism [72,73], the CF between two particles with a relative momentum $\vec{p}$ can be expressed as

$$C(\vec{p}) = \int d^3r\, S(\vec{r})|\Psi^{(-)}(\vec{p}, \vec{r})|^2, \quad (9)$$

where $S(\vec{r})$ denotes the source distribution of the relative separation between the two emitted particles at chemical freeze-out, and $\Psi^{(-)}(\vec{p}, \vec{r})$ is the outgoing two-body wave

function that encodes the final-state interaction. Assuming a spherically symmetric Gaussian source,

$$S(r) = \frac{1}{(4\pi R^2)^{3/2}} \exp\left(-\frac{r^2}{4R^2}\right), \tag{10}$$

where R characterizes the source size, the CF depends only on the modulus of the relative momentum $p = |\vec{p}|$.

For coupled-channel systems, such as the VP meson pairs considered here, Eq. (9) generalizes to [50]

$$C_i(p) = \sum_j w_j \int d^3r\, S_j(r) |\Psi^{(-)}_{ji}(p, r)|^2, \tag{11}$$

where the indices i and j label the detection and coupled intermediate channels, respectively. The outgoing wave function $\Psi^{(-)}_{ji}$ satisfies the Lippmann-Schwinger (Bethe-Salpeter) equation with an interaction potential V_{ji} derived from the on-shell unitarized T matrix in the chiral framework, ensuring consistency between the femtoscopic analysis and the scattering amplitudes that generate the $K_1(1270)$ poles. The explicit form of $\Psi^{(-)}_{ji}$ reads

$$\Psi^{(-)}_{ji}(p, r) = \delta_{ji} j_0(pr) + \int_0^{q_{\max}} \frac{d^3q}{(2\pi)^3} \frac{E(q) + \omega(q)}{E(q)\omega(q)} \times \frac{T_{ji}(\sqrt{s}, q, p)}{s(p) - [E(q) + \omega(q)]^2 + i\epsilon} j_0(qr). \tag{12}$$

Here, j_0 denotes the spherical Bessel function of the first kind. The quantities $E(q) = \sqrt{q^2 + M_j^2}$ and $\omega(q) = \sqrt{q^2 + m_j^2}$ represent the energies of the heavy matter particle (the vector meson) and the pseudoscalar meson in the initial-state channel j, respectively. The function $s(p)$ corresponds to the squared center-of-mass energy of the final-state channel i with relative momentum p. $q_{\max}$ represents a sharp ultraviolet cutoff that suppresses the high-energy components of the propagator.

In the present work, the strong interaction between the VP pairs is fully incorporated through the coupled-channel T-matrix $T^{\mathrm{S}}_{ji}(\sqrt{s})$ of the unitarized chiral perturbation theory in Eq. (3), while the Coulomb interaction $T^{\mathrm{C}}_{ii}(\sqrt{s}, q, p)$ in charged channels (e.g., ρ^+K^- and $K^{*-}\pi^+$) is included perturbatively $T_{ii}(\sqrt{s}, q, p) = T^{\mathrm{S}}_{ii}(\sqrt{s}) + T^{\mathrm{C}}_{ii}(\sqrt{s}, q, p)$ as described in Refs. [46,54].

III. RESULTS AND DISCUSSION

A. Fits of vector meson masses

According to the $\pi\pi$ and πK scattering phase shifts obtained from lattice QCD simulations performed by the Hadron Spectrum Collaboration (HSC) over the past decade [74–78], the masses of the ρ and K^* vector mesons can be extracted from the pole positions of parametrized scattering amplitudes evaluated at different pion and kaon masses. Note that while the decay width Γ is dynamically related to the mass m and the coupling g_{VPP} through Eq. (8), the input parameters from lattice QCD are treated as independent in the χ^2 analysis. Given that these pole parameters are extracted via a multistep procedure involving finite-volume spectra and amplitude analysis, which inherently carry significant systematic uncertainties, such a dynamical treatment is considered sufficiently robust for the current LO phenomenological study.

TABLE I. Tabulated quantities correspond to the pion mass m_π, kaon mass m_K, and the extracted ρ and K^* vector-meson pole parameters (all quantities in units of MeV) obtained from the HSC studies [74–78].

m_π	m_K	m_ρ	Γ_ρ	m_{K^*}	Γ_{K^*}
239	507.7 ± 2.4	783 ± 2	85.0 ± 2.0	902 ± 2	23 ± 2
283	519.4 ± 2.6	799 ± 2	59.7 ± 1.9	909 ± 4	13 ± 2
330	527.8 ± 2.8	815 ± 3	35.8 ± 1.8	914 ± 2	6 ± 1
391	549.1 ± 1.2	853 ± 2	12.4 ± 0.6	934 ± 2	0 ± 1

Based on the results summarized in Table I, we carry out a global fit that combines the HSC lattice QCD results with the corresponding experimental measurements, following the strategy outlined in Sec. II A.[1] In this fit, the kaon trajectory is described by the linear squared-mass relation in Eq. (6), whereas the ρ and K^* are modeled by the quadratic forms in Eq. (7) for their masses and couplings, which effectively capture the impact of their sizable decay widths. Since the HSC simulations were performed at a finite spatial lattice spacing $a_{\mathrm{lat}} \sim 0.12$ fm (temporal spacing a_t is used for the scale setting) [74–78], we include an a^2_{lat} term to account for discretization corrections and to provide continuum limit inputs to the UChPT framework. The fit parameters obtained from this global analysis are listed in Table II, and the corresponding curves with the 1σ uncertainty bands are shown in Fig. 1. The resulting masses and couplings as functions of m_π are then used as input to the coupled-channel UChPT study in the next Section.

For the sake of completeness, we also consider the case of mass evolution fits with the inclusion of the m_π^3 term in Eq. (7). Although the χ^2/d.o.f of the fit decreases, there is no significant change to the two-pole trajectories as described in Sec. III B, with the pole positions shifting by only ± 5 MeV. The only minor discrepancy arises when m_π approaches 600 MeV, where the effect of the m_π^3 term becomes slightly more pronounced, even though this is almost beyond the range of m_π we are interested in.

[1]Note that the HSC does not provide scattering data at different lattice spacings, and therefore this assumption in Eq. (7) should be verified in future lattice QCD simulations.

TABLE II. Fit coefficients and the corresponding reduced chi-squared (χ^2/d.o.f) for the m_π dependence of pseudoscalar and vector meson masses and couplings. All physical quantities are expressed in appropriate powers of GeV.

Particle	χ^2/d.o.f.	Parameter	Value ± Uncertainty	Unit
K	0.32	a_K	0.23697 ± 0.00048	GeV^2
		b_K	0.454 ± 0.025	1
		c_K	-0.0137 ± 0.0075	GeV^4
ρ	1.44	$c_0^{(\rho)}$	0.7609 ± 0.0010	GeV
		$c_1^{(\rho)}$	0.740 ± 0.027	GeV^{-1}
		$c_2^{(\rho)}$	-0.0576 ± 0.0070	GeV^3
		$\tilde{c}_0^{(\rho)}$	5.939 ± 0.054	1
		$\tilde{c}_1^{(\rho)}$	0.60 ± 1.8	GeV^{-2}
		$\tilde{c}_2^{(\rho)}$	-0.71 ± 0.34	GeV^2
K^*	1.27	$c_0^{(K^*)}$	0.8854 ± 0.0021	GeV
		$c_1^{(K^*)}$	0.330 ± 0.029	GeV^{-1}
		$c_2^{(K^*)}$	-0.0101 ± 0.0091	GeV^3
		$\tilde{c}_0^{(K^*)}$	5.61 ± 0.21	1
		$\tilde{c}_1^{(K^*)}$	-1.6 ± 9.1	GeV^{-2}
		$\tilde{c}_2^{(K^*)}$	-1.4 ± 1.4	GeV^2

B. Two-pole trajectories

In Ref. [17], the coupled-channel analysis of the VP interaction was performed within the leading-order unitarized chiral perturbation theory. Two poles were dynamically generated, located just below the ρK threshold and slightly above the $K^*\pi$ threshold, respectively. When the three higher channels are neglected, the essential features of the spectrum remain unchanged. By slightly readjusting the subtraction constants to $a_{K^*\pi} = -2.21$ and $a_{\rho K} = -2.44$ while keeping $\mu = 900$ MeV and $f = 115$ MeV, one obtains nearly identical pole positions at $W_H = 1269.5 - 12.0i$ MeV and $W_L = 1198.5 - 123.2i$ MeV for the zero-width case [35]. For comparison, if we keep the same set of subtraction constants as above, the pole positions shift to $W_H = 1289.2 - 154.0i$ MeV and $W_L = 1192.6 - 113.3i$ MeV in the finite-width case. The sizable shift of the higher pole is of kinematical origin and does not affect the underlying two-channel dynamics [17], as will be illustrated by the pole trajectories. This demonstrates that the dominant dynamics of the $K_1(1270)$ resonance are already well captured by the reduced two-channel system composed of ρK and $K^*\pi$.

Motivated by this observation, we perform the present calculation in the same unitarized chiral framework, restricting ourselves to the ρK and $K^*\pi$ coupled channels. The rationale for this simplification is twofold. First, as will be demonstrated in Sec. II B through the study of femtoscopic CFs, the dominant contributions to the femtoscopic line shapes arise from these two channels, whose distinct line shapes reflect their different coupling strengths [35]. Second, from the lattice-QCD perspective, simulating multichannel scattering involving unstable vector mesons such as ρ and K^* is extremely challenging, and current simulations are limited to systems composed of stable hadrons at relatively low pion masses [39,40]. Therefore, the two-channel approximation provides both a physically motivated and practically tractable description of the $K_1(1270)$ dynamics.

Furthermore, the essential difference between the $K_1(1270)$ system and the other well-known two-pole structure, the $\Lambda(1405)$ [35], lies in the fact that the heavy scattering constituents in the former case, ρ and K^*, are themselves resonances with large decay widths and short lifetimes. To clarify the chiral trajectories of the lower and higher poles, we perform calculations in two scenarios: one neglecting and one incorporating the vector meson decay widths. We expect that the qualitative evolution behavior of the poles is largely independent of whether or not the vector-meson widths are explicitly included. Fortunately, the unitarized chiral framework provides a straightforward way to incorporate the finite widths and spin properties of the ρ and K^* mesons by modifying the analytic form of the loop functions as described in Sec. II A.

In Fig. 2, we show the resulting chiral trajectories of the two poles. The left panel corresponds to the lower pole, which couples predominantly to the $K^*\pi$ channel, while the right panel corresponds to the higher pole, mainly

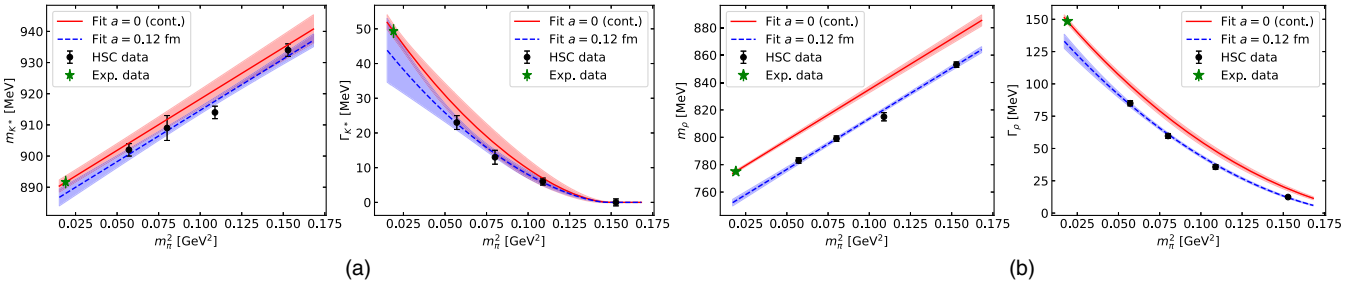


FIG. 1. (a) Chiral extrapolation of the K^* mass and decay width; (b) chiral extrapolation of the ρ mass and decay width. The solid and dashed lines denote the continuum-limit and the discrete lattice QCD fits, respectively, and the shaded regions correspond to the 1σ uncertainty bands.

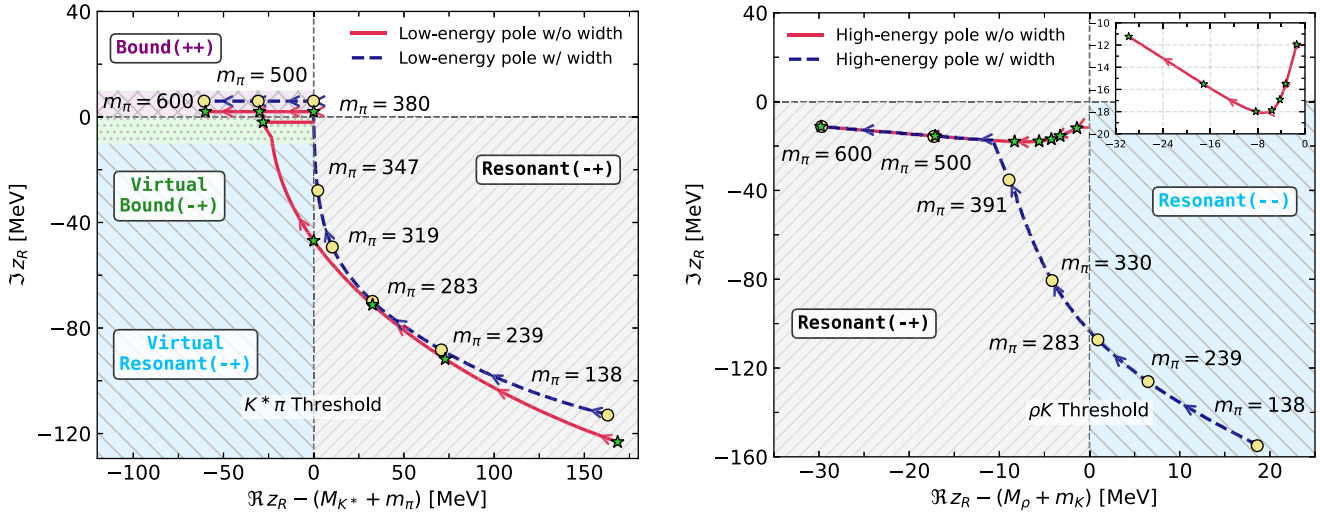


FIG. 2. Chiral evolution of the two-pole structure of the $K_1(1270)$ resonance in the ρK–$K^*\pi$ coupled-channel system. The left and right panels correspond to the lower and higher poles, mainly coupled to $K^*\pi$ and ρK, respectively. Solid and dashed lines denote the results without and with finite vector-meson widths, respectively. Markers indicate pole positions at different pion masses, with the critical masses explicitly labeled. In this context, bound states are located on the real axis of the first Riemann sheet $(++)$ below the $K^*\pi$ threshold, while virtual bound states are on the real axis of the second Riemann sheet $(-+)$ below the same threshold. Virtual resonant states refer to states on the second Riemann sheet $(-+)$ below the $K^*\pi$ threshold but with a finite width (nonzero imaginary part). Other resonances are located either on the second Riemann sheet $(-+)$ above the $K^*\pi$ threshold but below the ρK threshold, or on the other Riemann sheet $(--)$ above the ρK threshold.

associated with the ρK channel. The evolution of both poles is consistent with that reported in Ref. [35] for the $\Lambda(1405)$, highlighting their common origin from chiral dynamics. In both subfigures, different pion-mass values along the trajectories are indicated by stars or circles.

In the left panel, the lower pole exhibits a characteristic behavior: as the pion mass increases, the strength of the WT interaction grows, causing the pole to move from an above-threshold resonance to a below-threshold virtual or bound state. In the case without vector-meson widths, the trajectory undergoes a "zigzag" evolution: the resonance first becomes a below-threshold state located on the second Riemann sheet $(-+)$, then evolves into a virtual state as the width decreases to zero, and eventually crosses to the first Riemann sheet $(++)$ as a zero-energy bound state before becoming a deeply bound state as the binding energy increases [35]. When the widths are included, the pole instead evolves directly from an above-threshold resonance to a bound state without exhibiting the zigzag pattern, in agreement with the general expectation discussed in Ref. [79].

The right panel shows a much simpler pattern for the higher pole, consistent with the findings of Ref. [35]. As the pion mass increases, the attraction in the ρK channel strengthens, and the higher pole moves downward in energy, following a more intuitive trajectory. The main difference between the two scenarios lies in the physical starting point: in the case without width, the higher pole initially appears as a shallow below-threshold resonance, while in the width-included case, it starts as an above-threshold resonance with a larger imaginary part. Nevertheless, both treatments yield essentially the same qualitative two-pole trajectories, demonstrating that the inclusion of finite widths does not significantly alter the overall chiral evolution of the $K_1(1270)$ poles.

Since the vector-meson mass evolution formulas include uncertainties propagated from the fits to the lattice-QCD data [74–78], we also take into account the corresponding uncertainties in the pole trajectories. However, we do not explicitly display the error bands in Fig. 2, because the variations of the pole positions are relatively small—less than 5 MeV in both mass and width—and thus visually indistinguishable on the scale of the figure.

To address the potential uncertainties in the pole trajectories arising from the choice of parameters (a, μ, and f), we provide the following clarifications. In our framework, these three parameters are determined by fitting to experimental data [17]. Within the EFT power-counting scheme, the primary source of theoretical uncertainty stems from the truncation of higher-order (next-to-leading order (NLO) and beyond) contributions [34,80–83]. In this exploratory LO study, the systematic error from neglecting these higher-order effects is expected to outweigh the statistical uncertainties in the LO parameters. Specifically, while the decay constant f and the subtraction constant $a(\mu)$ are formally dependent on the pion mass m_π, a consistent incorporation of their chiral extrapolation would require additional LECs from NLO or higher orders [41,84]. Due to the lack of sufficient experimental or lattice constraints at unphysical quark masses, any specific heuristic choice for the evolution

of $a(\mu)$ (e.g., threshold conditions or cutoff matching [14,24,85]) would introduce additional model dependence. Given that the two-pole structure is a robust consequence of chiral dynamics at LO—as evidenced in the $\Lambda(1405)$ sector [35] and recent comparisons with Lattice QCD [39,40]—we maintain the established three-parameter framework to ensure a concise and physically grounded description of the $K_1(1270)$ pole trajectories.

C. Femtoscopic correlation functions

Since the femtoscopic CF is a direct experimental observable, it is necessary to convert the theoretical amplitudes from the isospin basis, which is more suitable for lattice-QCD studies with an $N_f = 2 + 1$ flavor setup [38], to the charge basis, which corresponds to experimentally measurable final states [13]. The $K_1(1270)$ forms an isospin doublet with two members, $K_1^0(1270)$ [27,28] and $K_1^-(1270)$ [17,26]. For $I_3 = +1/2\,(Q = 0)$, the channels are $\{\rho^+K^-, \rho^0\bar{K}^0, \bar{K}^{*0}\pi^0, K^{*-}\pi^+, \omega\bar{K}^0, \bar{K}^{*0}\eta, \phi\bar{K}^0\}$, while for $I_3 = -1/2\,(Q = -1)$ they are $\{\rho^0K^-, \rho^-\bar{K}^0, K^{*-}\pi^0, \bar{K}^{*0}\pi^-, \omega K^-, K^{*-}\eta, \phi K^-\}$.

To include the finite-width effects of the vector mesons, we adopt the formalism developed in Ref. [53], which consistently accounts for the widths both in the T matrix and in the asymptotic final-state relative wave functions, ultimately yielding modified femtoscopic CFs. For the $I_3 = +1/2$ case, in addition to the strong interactions that are common to both isospin components, the electromagnetic Coulomb interaction must also be considered due to the presence of the charged channels ρ^+K^- and $K^{*-}\pi^+$. The implementation of the Coulomb contribution follows the prescriptions given in Sec. II B, where it is incorporated perturbatively by adding the Coulomb amplitudes to the diagonal strong scattering amplitudes in the same manner as a Born-term correction.

We summarize here the relevant parameters employed in the calculation of the femtoscopic CFs. First, the source size R is taken to be three representative values $R = 1, 2, 3$ fm. Second, the channel weights w_j, which quantify the relative contributions from various coupled channels, are set to unity for simplicity. Third, the subtraction constants, renormalization scale, and decay constant are chosen to be consistent with those adopted in Ref. [17], namely

$$\mu = 900\ \text{MeV}, \qquad a(\mu) = -1.85, \qquad f = 115\ \text{MeV}, \tag{13}$$

where μ denotes the renormalization scale, $a(\mu)$ is the universal subtraction constant, and f represents the pion decay constant. These parameter choices follow the convention established in previous analyses of the $K_1(1270)$ system [26–28] and ensure consistency with the chiral interaction framework used throughout this study. Finally, to estimate the theoretical uncertainties, we vary the cutoff $q_{\max}$ in Eq. (12) within a reasonable range of 0.6–1.4 GeV. This variation is consistent with the typical choice of the subtraction constant $a(\mu)$, and corresponds to the equivalent cutoff Λ in the cutoff regularization scheme of the T matrix [15].

Specifically, setting these weights w_j to unity is a common practice in exploratory theoretical studies at LO [44,45,47,48]. In principle, these weights are not universal and depend heavily on the specific production environment. This information is typically accessible only through high-precision experimental measurements such as K^-p CFs [86,87]. Moreover, significant correlations exist between the channel weights w_j and the source size R [42]. Without

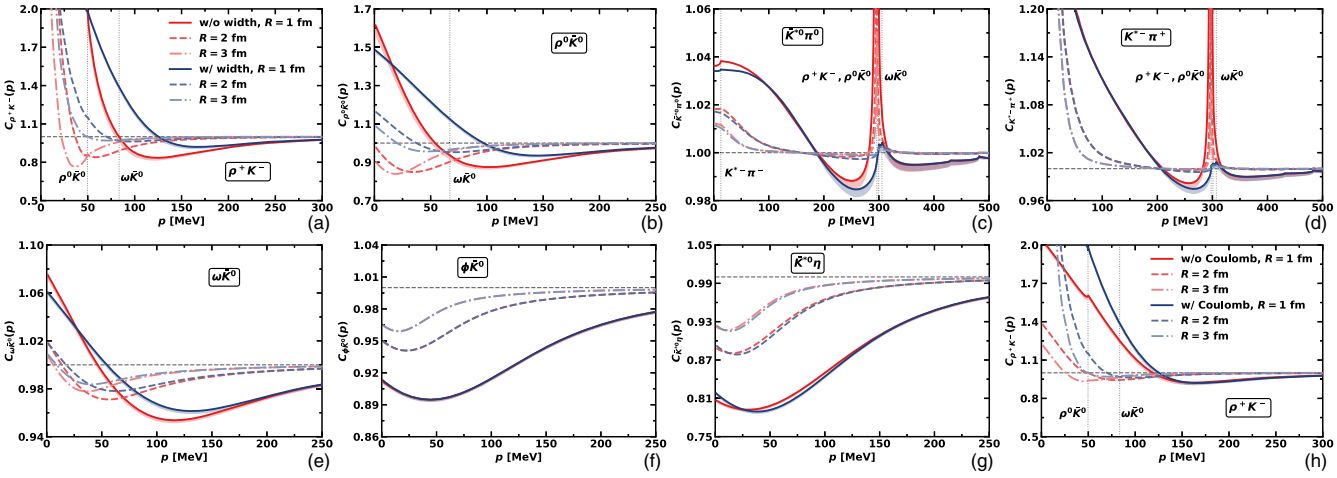


FIG. 3. Femtoscopic correlation functions $C_i(p)$ for the $Q = 0$ sector. Panels (a)–(g) show results for the individual coupled channels: $\{\rho^+K^-, \rho^0\bar{K}^0, \bar{K}^{*0}\pi^0, K^{*-}\pi^+, \omega\bar{K}^0, \bar{K}^{*0}\eta, \phi\bar{K}^0\}$. Panel (h) focuses specifically on the ρ^+K^- channel to illustrate the impact of the Coulomb interaction. The red and blue curves represent results without and with vector-meson widths, respectively, and different line styles and transparencies correspond to source sizes of $R = 1, 2$, and 3 fm.

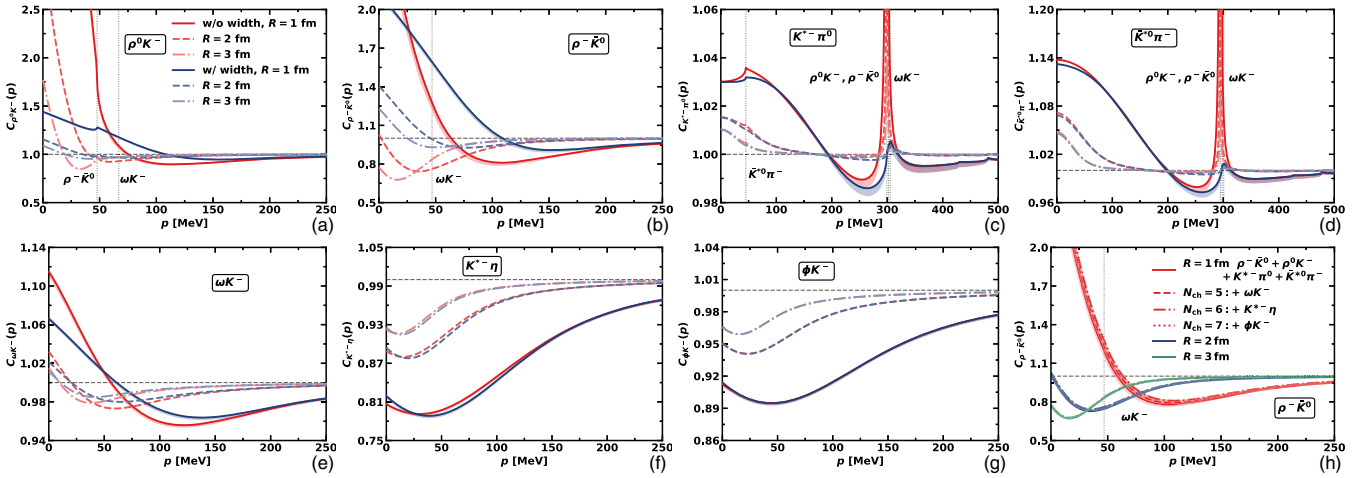


FIG. 4. Femtoscopic correlation functions $C_i(p)$ for the $Q=-1$ sector. Panels (a)–(g) show results for the individual coupled channels: $\{\rho^0K^-, \rho^-\bar{K}^0, K^{*-}\pi^0, \bar{K}^{*0}\pi^-, \omega K^-, K^{*-}\eta, \phi K^-\}$. Panel (h) illustrates the sensitivity of the $C_{\rho^-\bar{K}^0}$ correlation function to the inclusion of the sequential addition of channels ($\rho\bar{K}+\bar{K}^*\pi$, followed by $\omega\bar{K}$, $\bar{K}^*\eta$, and $\phi\bar{K}$). The red and blue curves represent results without and with vector-meson widths, respectively, and different line styles and transparencies correspond to source sizes of $R=1$, 2, and 3 fm.

further experimental constraints, fine-tuning these weights would introduce additional uncontrolled parameters and model dependence. Therefore, we adopt this uniform-weight scheme to provide a transparent baseline for the unitarized chiral dynamics.

In Figs. 3 and 4, we show the calculated CFs for the seven final-state channels in the two charge bases $Q=0$ and $Q=-1$, respectively. For each channel, the CF $C_i(p)(i=1,\ldots,7)$ is plotted over the relative momentum range (0, 250) MeV, except for the $\bar{K}^*\pi$ channels, for which the range (0, 500) MeV is adopted to illustrate better the threshold cusps induced by the coupled $\rho\bar{K}$ and $\omega\bar{K}$ channels. These cusp structures are significantly smoothed when the vector-meson decay widths are included. The threshold effects from the higher channels $\bar{K}^*\eta$ and $\phi\bar{K}$ are omitted in all plots, as their influence on the line shapes of the CFs is negligible.

In both Figs. 3 and 4, two sets of curves are shown using distinct color schemes: the red curves correspond to calculations without including the vector-meson widths, and the blue curves include the width effects. Within each color set, different source sizes $R=1,2,3$ fm are plotted with decreasing opacity. From the first five subfigures (a) to (e), one can observe that the red curves are much sharper than the blue ones. This behavior reflects that incorporating the finite widths of the intermediate vector mesons effectively smears the loop functions, resulting in smoother scattering amplitudes. The only exceptions are the highest-threshold channels, $\bar{K}^*\eta$ and $\phi\bar{K}$, where the couplings to the lower channels are weak, as evident from the potential-coefficient matrix C_{ij} in Eq. (2).

Within each color system, increasing the source size R systematically weakens the interaction strength, leading to a corresponding reduction in the magnitude of the CF, as expected from the standard source-size dependence in Femtoscopy [42,48].

Comparing the subfigures (a) to (f) for different final-state channels, one can see that for the five lower-threshold channels, the CFs exhibit resonantlike behavior, consistent with the findings of Refs. [47,52]. In contrast, for the last two channels, $\bar{K}^*\eta$ and $\phi\bar{K}$, the line shapes resemble those of weakly bound states due to the small coupling between the two poles and these higher channels.

Turning to the $Q=0$ sector in Fig. 3, a pronounced enhancement appears in the low-momentum region of the CFs in channels ρ^+K^- and $K^{*-}\pi^+$, as compared with their isospin-partner channels ρ^0K^- and $\bar{K}^{*0}\pi^-$ in Fig. 4 [42]. This enhancement originates predominantly from the Coulomb interaction rather than from small isospin-breaking effects. While the low-momentum enhancement is a general feature arising from the attractive nature of the $\rho\bar{K}$ and $\bar{K}^*\pi$ interactions, the additional boost in the $Q=0$ sector originates predominantly from the attractive Coulomb interaction between oppositely charged hadrons. This Coulomb-induced effect becomes significantly more prominent when finite vector-meson widths are included, as shown in panel (a), in contrast between Figs. 3 and 4. The inclusion of finite widths tends to smooth the overall correlation pattern, thereby highlighting the distinct Coulomb-induced enhancement against the background. To further illustrate this behavior, the last subfigure (h) in Fig. 3 shows the ρ^+K^- CF with and without the Coulomb interaction, both calculated including the finite vector-meson widths. The comparison confirms that the Coulomb force produces a strong near-threshold enhancement, whereas the finite widths mainly smooth the overall correlation pattern.

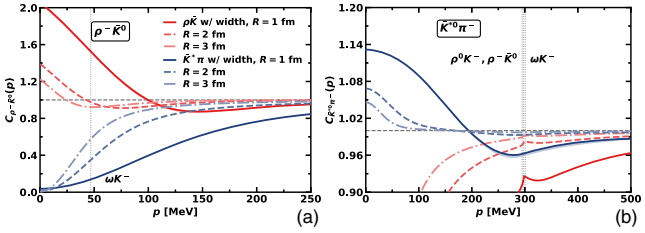


FIG. 5. Femtoscopic correlation functions $C_i(p)$ for the two channels $\rho^-\bar{K}^0$ and $\bar{K}^{*0}\pi^-$ in the $Q=-1$ system. The red and blue lines represent the individual contributions to $C(p)$ from the $\rho\bar{K}$ and $\bar{K}^*\pi$ channels, respectively. Different line styles and transparencies correspond to source radii of $R=1,2$, and 3 fm.

In the last subfigure (h) of the $Q=-1$ sector of Fig. 4, three color groups (red, blue, and green) represent source sizes of $R=1,2,3$ fm, respectively. Within each group, we sequentially add channels to the coupled system with finite widths: starting with only $\rho\bar{K}$ and $\bar{K}^*\pi$, and including $\omega\bar{K}$, $\bar{K}^*\eta$, and $\phi\bar{K}$ [42,48], one by one. The resulting curves lie nearly on top of one another, with only minor increases in magnitude as additional channels are introduced. This confirms that restricting the analysis to the dominant two channels, $\rho\bar{K}$ and $\bar{K}^*\pi$, is a justified and physically sound approximation [35].

Finally, to clarify more precisely the connection between the two-pole structure and the femtoscopic CFs, we focus on two representative channels, $\rho^-\bar{K}^0$ and $\bar{K}^{*0}\pi^-$, from the $Q=-1$ system, and calculate the individual contributions from the $\rho\bar{K}$ and $\bar{K}^*\pi$ components, respectively. From Fig. 5, one can clearly observe the distinct behavior of the two poles in different final states. In the left panel, the $\rho\bar{K}$ contribution is primarily governed by the higher pole, so that the red line exhibits a typical resonant behavior. In contrast, the $\bar{K}^*\pi$ contribution is mainly dominated by the lower pole, where the blue line gradually increases from zero and approaches unity, showing a clear signature of a deeply bound state relative to the $\rho^-\bar{K}^0$ threshold [52]. In the right panel, the situation is essentially reversed: the blue line almost entirely dominates the low-momentum region of the total CFs shown in Fig. 4, simply because the lower pole plays a crucial role in the $\bar{K}^*\pi$ component.

IV. CONCLUSION AND OUTLOOK

In this work, we have performed a comprehensive study of the axial-vector resonance $K_1(1270)$ within the two-pole scenario predicted by UChPT. Using a coupled-channel framework including the dominant ρK and $K^*\pi$ interactions, we reproduced the well-known two-pole structure originally identified in Refs. [17,35] and investigated its dependence on the light-quark masses. The fitted pion-mass evolution of the ρ and K^* vector mesons, constrained by both lattice-QCD and experimental data, enabled us to trace the trajectories of the two poles in the complex-energy plane with increasing pion mass. We further examined the influence of vector-meson decay widths by comparing calculations with and without width effects, demonstrating that including finite widths smooths the pole evolution but does not alter the qualitative two-pole pattern.

The lower pole, dominantly coupled to the $K^*\pi$ channel, evolves from an above-threshold resonance to a bound or virtual state as the pion mass increases, while the higher pole, mainly associated with ρK, moves downward in energy, showing a strengthened attraction consistent with chiral expectations. These results establish a consistent and physically intuitive picture of the chiral evolution of the $K_1(1270)$ two-pole structure.

In addition, we have carried out a detailed analysis of the femtoscopic CFs for all relevant VP channels in both charge sectors. The calculated CFs clearly reflect the two-pole dynamics and exhibit distinct resonance and bound-state features in different channels. We have also shown that the vector meson finite widths play a smoothing role in the CF line shapes, and that the Coulomb interaction produces sizable low-momentum enhancements in the charged channels ρ^+K^- and $K^{*-}\pi^+$. Moreover, the negligible influence of the higher channels such as $\omega\bar{K}$, $\bar{K}^*\eta$, and $\phi\bar{K}$ further confirms that the simplified two-channel description (ρK, $K^*\pi$) captures the essential dynamics of the $K_1(1270)$ system.

Future directions include the extension of the present framework to incorporate additional coupled channels with improved lattice QCD constraints, as well as the direct comparison of the predicted CFs with experimental measurements from ALICE and future facilities. Such developments will allow a more precise determination of the $K_1(1270)$ pole parameters and a deeper understanding of its molecular components, offering valuable insight into the nonperturbative dynamics of chiral symmetry breaking and resonance formation in QCD.

ACKNOWLEDGMENTS

This work is partly supported by the National Key R&D Program of China under Grant No. 2023YFA1606703 and the National Natural Science Foundation of China under Grants No. 12435007 and No. 12105006. Z. W. L. acknowledges support from the National Natural Science Foundation of China under Grants No. 12405133, No. 12347180, China Postdoctoral Science Foundation under Grant No. 2023M740189, and the Postdoctoral Fellowship Program of CPSF under Grant No. GZC20233381. H. L. acknowledges the JSPS Grant-in-Aid for Scientific Research (S) under Grant No. JP20H05648. R. M. acknowledges support from the ESGENT program (ESGENT/018/2024) and the PROMETEU program (CIPROM/2023/59), of the Generalitat Valenciana, and also from the Spanish

Ministerio de Economia y Competitividad (MINECO) and European Union (NextGenerationEU/PRTR) by the Grants with Ref. No. CNS2022-136146, and Ref. No. PID2023-147458NB-C21.

DATA AVAILABILITY

The data are not publicly available. The data are available from the authors upon reasonable request.

[1] N. Brambilla *et al.*, Eur. Phys. J. C **71**, 1534 (2011).
[2] H.-X. Chen, W. Chen, X. Liu, and S.-L. Zhu, Phys. Rep. **639**, 1 (2016).
[3] J.-M. Richard, Few Body Syst. **57**, 1185 (2016).
[4] A. Esposito, A. Pilloni, and A. D. Polosa, Phys. Rep. **668**, 1 (2017).
[5] R. F. Lebed, R. E. Mitchell, and E. S. Swanson, Prog. Part. Nucl. Phys. **93**, 143 (2017).
[6] A. Hosaka, T. Hyodo, K. Sudoh, Y. Yamaguchi, and S. Yasui, Prog. Part. Nucl. Phys. **96**, 88 (2017).
[7] F.-K. Guo, C. Hanhart, U.-G. Meißner, Q. Wang, Q. Zhao, and B.-S. Zou, Rev. Mod. Phys. **90**, 015004 (2018); **94**, 029901(E) (2022).
[8] S. L. Olsen, T. Skwarnicki, and D. Zieminska, Rev. Mod. Phys. **90**, 015003 (2018).
[9] M. Karliner, J. L. Rosner, and T. Skwarnicki, Annu. Rev. Nucl. Part. Sci. **68**, 17 (2018).
[10] Y.-R. Liu, H.-X. Chen, W. Chen, X. Liu, and S.-L. Zhu, Prog. Part. Nucl. Phys. **107**, 237 (2019).
[11] M. Mai, U.-G. Meißner, and C. Urbach, Phys. Rep. **1001**, 1 (2023).
[12] H.-X. Chen, W. Chen, X. Liu, Y.-R. Liu, and S.-L. Zhu, Rep. Prog. Phys. **86**, 026201 (2023).
[13] M.-Z. Liu, Y.-W. Pan, Z.-W. Liu, T.-W. Wu, J.-X. Lu, and L.-S. Geng, Phys. Rep. **1108**, 1 (2025).
[14] M. F. M. Lutz and E. E. Kolomeitsev, Nucl. Phys. **A730**, 392 (2004).
[15] L. Roca, E. Oset, and J. Singh, Phys. Rev. D **72**, 014002 (2005).
[16] S. Godfrey and N. Isgur, Phys. Rev. D **32**, 189 (1985).
[17] L. S. Geng, E. Oset, L. Roca, and J. A. Oller, Phys. Rev. D **75**, 014017 (2007).
[18] S. Weinberg, Phys. Lett. B **251**, 288 (1990).
[19] N. Kaiser, P. B. Siegel, and W. Weise, Nucl. Phys. **A594**, 325 (1995).
[20] N. Kaiser, T. Waas, and W. Weise, Nucl. Phys. **A612**, 297 (1997).
[21] E. Oset and A. Ramos, Nucl. Phys. **A635**, 99 (1998).
[22] J. A. Oller, E. Oset, and A. Ramos, Prog. Part. Nucl. Phys. **45**, 157 (2000).
[23] T. Hyodo and D. Jido, Prog. Part. Nucl. Phys. **67**, 55 (2012).
[24] J. A. Oller, Prog. Part. Nucl. Phys. **110**, 103728 (2020).
[25] M. C. Birse, Z. Phys. A **355**, 231 (1996).
[26] G. Y. Wang, L. Roca, and E. Oset, Phys. Rev. D **100**, 074018 (2019).
[27] G.-Y. Wang, L. Roca, E. Wang, W.-H. Liang, and E. Oset, Eur. Phys. J. C **80**, 388 (2020).
[28] J. M. Dias, G. Toledo, L. Roca, and E. Oset, Phys. Rev. D **103**, 116019 (2021).
[29] L. Roca, W. H. Liang, and E. Oset, Phys. Lett. B **824**, 136827 (2022).
[30] S. Navas *et al.* (Particle Data Group), Phys. Rev. D **110**, 030001 (2024).
[31] J. A. Oller and U.-G. Meißner, Phys. Lett. B **500**, 263 (2001).
[32] D. Jido, J. A. Oller, E. Oset, A. Ramos, and U. G. Meissner, Nucl. Phys. **A725**, 181 (2003).
[33] U.-G. Meißner, Symmetry **12**, 981 (2020).
[34] J.-X. Lu, L.-S. Geng, M. Doering, and M. Mai, Phys. Rev. Lett. **130**, 071902 (2023).
[35] J.-M. Xie, J.-X. Lu, L.-S. Geng, and B.-S. Zou, Phys. Rev. D **108**, L111502 (2023).
[36] J.-M. Xie, J.-X. Lu, L.-S. Geng, and B.-S. Zou, EPJ Web Conf. **303**, 01011 (2024).
[37] J.-M. Xie, J.-X. Lu, L.-S. Geng, and B.-S. Zou, Proc. Sci., CD2024 (**2026**) 005 [arXiv:2504.03392].
[38] R. A. Briceno, J. J. Dudek, and R. D. Young, Rev. Mod. Phys. **90**, 025001 (2018).
[39] J. Bulava *et al.* (Baryon Scattering (BaSc) Collaboration), Phys. Rev. Lett. **132**, 051901 (2024).
[40] J. Bulava *et al.* (Baryon Scattering (BaSc) Collaboration), Phys. Rev. D **109**, 014511 (2024).
[41] Z. Zhuang, R. Molina, J.-X. Lu, and L.-S. Geng, Sci. Bull. **70**, 1953 (2025).
[42] Y. Kamiya, T. Hyodo, K. Morita, A. Ohnishi, and W. Weise, Phys. Rev. Lett. **124**, 132501 (2020).
[43] Z.-W. Liu, K.-W. Li, and L.-S. Geng, Chin. Phys. C **47**, 024108 (2023).
[44] I. Vidana, A. Feijoo, M. Albaladejo, J. Nieves, and E. Oset, Phys. Lett. B **846**, 138201 (2023).
[45] N. Ikeno, G. Toledo, and E. Oset, Phys. Lett. B **847**, 138281 (2023).
[46] J. M. Torres-Rincon, À. Ramos, and L. Tolos, Phys. Rev. D **108**, 096008 (2023).
[47] Z.-W. Liu, J.-X. Lu, and L.-S. Geng, Phys. Rev. D **107**, 074019 (2023).
[48] Z.-W. Liu, J.-X. Lu, M.-Z. Liu, and L.-S. Geng, Phys. Rev. D **108**, L031503 (2023).
[49] R. Molina, Z.-W. Liu, L.-S. Geng, and E. Oset, Eur. Phys. J. C **84**, 328 (2024).
[50] M. Albaladejo, A. Feijoo, J. Nieves, E. Oset, and I. Vidaña, Phys. Rev. D **110**, 114052 (2024).
[51] V. M. Sarti, A. Feijoo, I. Vidaña, A. Ramos, F. Giacosa, T. Hyodo, and Y. Kamiya, Phys. Rev. D **110**, L011505 (2024).
[52] Z.-W. Liu, J.-X. Lu, M.-Z. Liu, and L.-S. Geng, Sci. Bull. **70**, 3515 (2025).
[53] A. Feijoo, M. Korwieser, and L. Fabbietti, Phys. Rev. D **111**, 014009 (2025).

[54] P. Encarnación, A. Feijoo, V. M. Sarti, and A. Ramos, Phys. Rev. D **111**, 114013 (2025).
[55] Z.-W. Liu, J.-X. Lu, and L.-S. Geng, Proc. Sci., QNP2024 (**2025**) 044.
[56] D.-L. Ge, Z.-W. Liu, J.-X. Lu, and L.-S. Geng, Phys. Rev. C **112**, 034003 (2025).
[57] Z.-W. Liu, D.-L. Ge, J.-X. Lu, M.-Z. Liu, and L.-S. Geng, Phys. Rev. D **112**, 054019 (2025).
[58] À. Ramos, J. M. Torres-Rincon, A. de Fagoaga, and E. Cabré, Phys. Rev. D **113**, 036020 (2026).
[59] Y.-b. Shen, Z.-W. Liu, J.-X. Lu, M.-Z. Liu, and L.-S. Geng, arXiv:2506.23476.
[60] Z.-H. Guo and J. A. Oller, Phys. Rev. C **87**, 035202 (2013).
[61] A. Cieplý, M. Mai, U.-G. Meißner, and J. Smejkal, Nucl. Phys. **A954**, 17 (2016).
[62] X. L. Ren, L. S. Geng, J. Martin Camalich, J. Meng, and H. Toki, J. High Energy Phys. 12 (2012) 073.
[63] K. Yu, Y. Li, J.-J. Wu, D. B. Leinweber, and A. W. Thomas, Phys. Rev. D **109**, 034505 (2024).
[64] Z. Wang, D. B. Leinweber, C. Liu, L. Liu, P. Sun, A. W. Thomas, J.-j. Wu, H. Xing, and K. Yu (CLQCD Collaboration), J. High Energy Phys. 08 (2025) 064.
[65] X. Feng, K. Jansen, and D. B. Renner, Phys. Rev. D **83**, 094505 (2011).
[66] P. C. Bruns and U.-G. Meissner, Eur. Phys. J. C **40**, 97 (2005).
[67] J. A. Oller, E. Oset, and J. R. Pelaez, Phys. Rev. D **59**, 074001 (1999); **60**, 099906(E) (1999); **75**, 099903(E) (2007).
[68] A. Gomez Nicola and J. R. Pelaez, Phys. Rev. D **65**, 054009 (2002).
[69] C. Hanhart, J. R. Pelaez, and G. Rios, Phys. Rev. Lett. **100**, 152001 (2008).
[70] D. Guo, A. Alexandru, R. Molina, and M. Döring, Phys. Rev. D **94**, 034501 (2016).
[71] R. Molina and J. Ruiz de Elvira, J. High Energy Phys. 11 (2020) 017.
[72] S. E. Koonin, Phys. Lett. **70B**, 43 (1977).
[73] S. Pratt, T. Csorgo, and J. Zimanyi, Phys. Rev. C **42**, 2646 (1990).
[74] J. J. Dudek, R. G. Edwards, and C. E. Thomas (Hadron Spectrum Collaboration), Phys. Rev. D **87**, 034505 (2013); **90**, 099902(E) (2014).
[75] D. J. Wilson, J. J. Dudek, R. G. Edwards, and C. E. Thomas, Phys. Rev. D **91**, 054008 (2015).
[76] D. J. Wilson, R. A. Briceno, J. J. Dudek, R. G. Edwards, and C. E. Thomas, Phys. Rev. D **92**, 094502 (2015).
[77] D. J. Wilson, R. A. Briceno, J. J. Dudek, R. G. Edwards, and C. E. Thomas, Phys. Rev. Lett. **123**, 042002 (2019).
[78] A. Rodas, J. J. Dudek, and R. G. Edwards (Hadron Spectrum Collaboration), Phys. Rev. D **108**, 034513 (2023).
[79] T. Hyodo, Phys. Rev. Lett. **111**, 132002 (2013).
[80] R. J. Furnstahl, N. Klco, D. R. Phillips, and S. Wesolowski, Phys. Rev. C **92**, 024005 (2015).
[81] J. A. Melendez, S. Wesolowski, and R. J. Furnstahl, Phys. Rev. C **96**, 024003 (2017).
[82] J. A. Melendez, R. J. Furnstahl, D. R. Phillips, M. T. Pratola, and S. Wesolowski, Phys. Rev. C **100**, 044001 (2019).
[83] J.-X. Lu, C.-X. Wang, Y. Xiao, L.-S. Geng, J. Meng, and P. Ring, Phys. Rev. Lett. **128**, 142002 (2022).
[84] F.-K. Guo, Y. Kamiya, M. Mai, and U.-G. Meißner, Phys. Lett. B **846**, 138264 (2023).
[85] T. Hyodo, D. Jido, and A. Hosaka, Phys. Rev. C **78**, 025203 (2008).
[86] S. Acharya *et al.* (ALICE Collaboration), Phys. Rev. Lett. **124**, 092301 (2020).
[87] S. Acharya *et al.* (ALICE Collaboration), Eur. Phys. J. C **83**, 340 (2023).